VERSITA

Central European Journal of **Physics**

A parallel three-dimensional scour model to predict flow and scour below a submarine pipeline

Research Article

Muhammad S. Alam*, Liang Cheng

*School of civil and resource engineering, The University of Western Australia
35, Stirling HW, Crawley, WA 6009, Australia*

Abstract: A three-dimensional Lattice Boltzmann flow and scour model is developed to simulate time-dependent scour below a submarine pipeline. The proposed model presented in this paper is able to predict streamwise and spanwise propagations of scour with respect to lattice unit of time. It is evident from this study that the existence of a spiral vortex in the proximity of the span shoulder is quite noteworthy. It is revealed that the critical regime of the 2-D scour process is found to be up to one pipe diameter away in both directions from the middle of the unsupported length of pipelines. The equilibrium maximum scour depth and the shape of streamwise equilibrium scour hole compare well with the available experimental data. The speed of propagation of scour along the pipeline length maintains an almost constant rate, which is consistent with the experimental observations found in literature. In addition, it is seen that the scour slope at the shoulder region remains fairly constant throughout the whole scour process.

PACS (2008): 47.11.Qr, 47.27.nd, 47.27.Jv, 47.27.T

Keywords: lattice Boltzmann • scour • vortex shedding • massage passing interface • submarine pipeline
© Versita Sp. z o.o.

1. Introduction

Thousands of kilometers of pipeline are laid each year across offshore seabeds in order to meet the needs of an energy-hungry world. The modern offshore pipelines are usually laid across harsh terrains and reach hostile ocean depths to serve literally as a "life line" between storage units and storage fields. Without the existence of the vast and complex offshore pipeline system, the modern world would have been a very different place. Additionally, transporting petroleum and its by-products through

pipelines is probably the most reliable, safest and cost-effective means of transportation. In contrast to the massive advantages, the oil and gas pipelines are vulnerable to marine environment as any accidents within pipelines may cause oil or gas spills resulting in huge damage to marine life. Accidents happen to pipelines due to various factors. Development of pipeline spanning is one of them. Though pipelines are laid directly on the seabed, the turbulent nature of flow across the pipeline causes washing away of erodible seabed under severe environmental conditions [1]. As a consequence, a free span of pipeline is developed. The consequence is nothing but the failure of pipeline and it has severe impacts on both the marine environment and economy. Therefore, understanding the 3-D

*E-mail: alam@civil.uwa.edu.au

Springer

nature of scouring is very important from this aspect. But, it is very costly to construct a large set-up for the physical modelling of 3-D scouring. So, it is easier to investigate 3-D scouring phenomena around submarine pipelines numerically if a good 3-D scour model and enough computational resources are available. Unfortunately, numerical investigation of three dimensional scour around submarine pipelines employing the Lattice Boltzmann Method has remained untouched until now. The main reason behind it might be the lack of time-dependent scour model to simulate three dimensional sand particle movements. This is complicated by the huge demand for computational resources and time required for modelling such phenomena.

Study of local scour around pipelines has been carried out both numerically and experimentally by many researchers over the last three decades. Mao [2] investigated the scour process around pipelines and identified the role of vortices that exist both in front and the behind a pipeline. The effect of seepage flow below the pipe was also discussed in that paper. Sumer *et al.* [3] investigated the effect of lee-wake on scour underneath pipelines both experimentally and numerically. Their investigation showed that the scour downstream of the pipe is apparently governed by the action of wake flow. Sumer *et al.* [4] carried out an experimental study regarding the onset of scour below and self-burial of pipelines in currents/waves. They revealed that there exists a pressure difference between the upstream and downstream sides of a pipeline, which drives a seepage flow. When the seepage flow is excessive it becomes responsible for onset of scour below the pipeline. They also determined the critical condition corresponding to the onset of scour below pipelines in currents/waves. Gao *et al.* [5] investigated the coupling effects between pipeline vibration and sand scour numerically. Their study revealed that the equilibrium scour depth decreases with increasing initial gap-to-diameter ratio. They also concluded that the vibrating pipe may induce a deeper scour hole than the fixed pipe. Ushijima [6] developed a numerical model based on the arbitrary Lagrangian-Eulerian formulation in order to predict local scour caused by turbulent flow. He concluded that his numerical results of sand bed profiles compared well with the experimental data.

This paper is concerned with the three-dimensional scour process around submarine pipelines. The purpose of the present study is to investigate the spanwise and streamwise scour below pipelines and the flow field around them. A parallel LBGK scour model is developed where motion of sand particles represents MPCA (Multi-Particle Cellular Automata) and a Smagorinsky sub-grid model is employed in order to solve high Reynolds number turbulent flow. MPI (massage passing interface) is implemented in order

to split the computational domain into many parts and the C++ language was employed to run the computation of each sub-domain staying on separate but homogeneous computers.

This paper is organized in the following manner. First of all, the 3-D flow model is validated against cavity flow. Then, the 3-D flow model is implemented to predict the 3-D vortex shedding flow in the vicinity of isolated cylinder. Numerical results are compared with the available experimental and numerical results of other researchers found in literature. Finally, the 3-D scour model is employed in order to calculate the time development of scour underneath the pipelines. The numerical results are then compared with available experimental data and observations.

2. Material and methods

2.1. The flow model

2.1.1. Lattice Boltzmann method (LBM)

LBM is the representation of a simplified kinetic model where the macroscopic hydrodynamics of fluid is achieved from the physics of microscopic or mesoscopic processes. The base equation which constitutes LBM originated from the kinetic theory of ideal gases.

The complete discretized equation (discrete Boltzmann equation) with the time step ∂_t and space step $\partial\mathbf{r}$ can be written as:

$$f_i(\mathbf{r} + \mathbf{e}_i\partial_t, t + \partial_t) - f_i(\mathbf{r}, t) = -\frac{1}{\tau}\left[f_i(\mathbf{r}, t) - f_i^{eq}(\mathbf{r}, t)\right]. \quad (1)$$

In the above mentioned equation f represents the single particle distribution function, which is the probability of finding a fictitious fluid particle in the lattice space $\mathbf{r}$ at a time t along the discrete velocity direction of $\mathbf{e}_i$. The above equation is also termed the Lattice Boltzmann equation with BGK approximation or the LBGK model [7]. The left hand side of Eq. (1) is representing a streaming process whereas the right hand side depicts the relaxation to equilibrium. Therefore, the LBGK model consists of two basic steps:

1. collision step:

$$\tilde{f}_i(\mathbf{r}, t + \partial t) = f_i(\mathbf{r}, t) - \frac{1}{\tau}\left[f_i(\mathbf{r}, t) - f_i^{eq}(\mathbf{r}, t)\right], \quad (2)$$

2. streaming step:

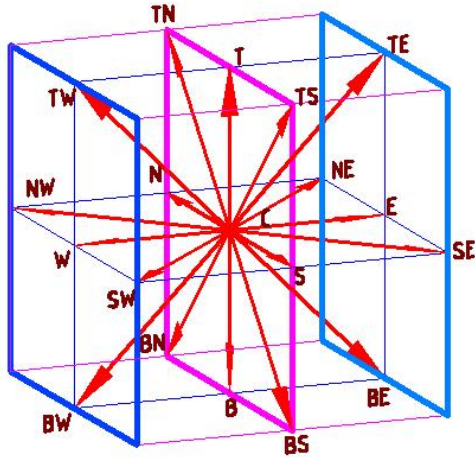$$f_i(\mathbf{r} + \mathbf{e}_i\partial_t, t + \partial_t) = \tilde{f}_i(\mathbf{r}, t + \partial t), \quad (3)$$

Figure 1. Lattice structure of D3Q19 model.

where $\tilde{f_i}$ represents the post collision state of the distribution function.

In that equation, f^{eq} is the equilibrium distribution function (the Maxwell distribution function) and τ is called the relaxation time, which governs the relaxation to equilibrium. Here, f^{eq} and can be written as:

$$f_i^{eq} = w_i\rho\left(1 + \frac{e_i.u}{c_s^2} + \frac{(e_i.u)^2}{2c_s^4} - \frac{u^2}{2c_s^2}\right),\tag{4}$$

where c_s is defined as $c/\sqrt{3}$. The lattice spacing and the discrete time step are assumed to be Δr and Δt respectively which yields $c = \Delta r/\Delta t$.

For, D3Q19 topology, the weighting factor $w_i\,(i \in \{0, 1, 2, 3, 4, 5, ..., 17, 18\})$ are:

$$w_i = \begin{cases} 1/3, & i = C, \\ 1/18, & i = N, S, E, W, T, B, \\ 1/36, & i = NE, NW, SE, SW, BE, BW, \\ & \quad BN, BS, TN, TS, TE, TW, \end{cases}$$

where, the capital letters indicate the discrete velocity space at: C(centre), N(north), S(south), E(east), W(west), T(top), B(bottom), NE(north-east), NW(north-west), SE(south-east), SW(south-west), BE(bottom-east), BW(bottom-west), BN(bottom-north), BS(bottom-south), TN(top-north), TS(top-south), TE(top-east), TW(top-west). Fig. 1 depicts the directional velocities with the above mentioned symbols for velocity vectors.

In addition, the definitions of e_i for D3Q19 model are:

$$e_i = \begin{cases} (0, 0, 0), & C, \\ (\pm 1, 0, 0)c, (0, \pm 1, 0)C, (0, 0, \pm 1)C, \\ \quad E, W, N, S, T, B, \\ (\pm 1, \pm 1, 0)c, (\pm 1, 0, \pm 1)c, (0, \pm 1, \pm 1)c, \\ \quad NE, NW, SE, SW, TE, BE, \\ \quad TS, BS, TN, BN, TS, BS. \end{cases}\tag{5}$$

The macroscopic fluid variables density $\rho(r, t)$ and momentum $\rho(r, t)\,u(r, t)$ are calculated as the first two moments of the distribution functions. They can be expressed as:

$$\rho(r, t) = \sum_i^{f_i},\tag{6}$$

$$\rho u = \sum_i^{e_i f_i}.\tag{7}$$

The kinematic shear viscosity is

$$v = \left(\frac{2\tau - 1}{6}\right) \times \frac{\Delta r^2}{\Delta t}.\tag{8}$$

Therefore, it is crystal clear that the governing equations of LBGK model are of a very simple form and the implementation is noticeably advantageous. Moreover, as the calculation of a collision step for a specific node requires only its own data, the computation is completely local. Furthermore, the streaming step calculation also requires very little computational effort. Once again, it is necessary to mention that unlike the traditional methods the pressure is calculated from the equation of state. So, pressure is calculated from the local data, whereas in the case of traditional methods global data communication is essential for solving the Poisson equation for the pressure. In addition, the Eq. (1) is very explicit and straightforward to parallelize. Due to the simplicity of the LBGK model, it provides a very short, straightforward and easy to implement algorithm. For more advantages of LBGK over the NS solvers, readers are referred to [8].

2.1.2. Turbulent model for flow stability

If we assume the size of lattice spacing, $\Delta r = 1$ and time step $\Delta t = 1$ then Eq. (8) can be rewritten as:

$$v = \frac{2\tau - 1}{6}.\tag{9}$$

Again, flow is characterized by the Reynolds number,

$$Re = \frac{UL}{v} = \frac{UL}{\frac{2\tau - 1}{6}}, \quad \text{where } \tau > \frac{1}{2}.\tag{10}$$

Therefore, if flow simulation at high Reynolds numbers is expected for a specific characteristic velocity and length,

the relaxation time (τ) has to be small. It should be noted that instabilities appear when the value of τ is lower than or approximately equal to 0.60 [9]. Hou *et al.* [10], proposed a sub-grid turbulent model for LBGK models in order to get ride of instabilities for high Reynolds number fluid flow applications. The main idea is to enhance the relaxation time by adding a new term v_t to the physical kinematic viscosity v. Thus, the total viscosity becomes,

$$v_{total} = v + v_t. \tag{11}$$

Here, v_t is termed as Smagorinsky eddy viscosity or turbulent viscosity and can be expressed as:

$$v_t = \left(C_{smago}\Delta\right)^2 |S|, \tag{12}$$

where, Δ is the filter size which represents the value of lattice spacing, C_{smago} is the Smagorinsky constant, and $|S|$ is the magnitude of the strain tensor which equals to $\sqrt{2S_{\alpha\beta}S_{\alpha\beta}}$ (where, $S_{\alpha\beta} = 1/2\left(\partial_\alpha \mathbf{u}_\beta + \partial_\beta \mathbf{u}_\alpha\right)$). To get the modified relaxation time τ_{total} , first the non-equilibrium stress tensor $\prod_{\alpha\beta}$ is computed locally as

$$\prod_{\alpha\beta} = \sum_i \mathbf{e}_{i\alpha}\mathbf{e}_{i\beta}(f_i - f_i^{eq}). \tag{13}$$

Then, for D3Q19 LBGK model, as in [9, 11], $S_{\alpha\beta}$ and v_t can be calculated as

$$S_{\alpha\beta} = -\frac{1}{2\rho\tau_{total}\Delta t}3\prod_{\alpha\beta}, \tag{14}$$

$$v_t = \frac{1}{\sqrt{2}\rho\tau_{total}\Delta t}9\left(C_{smago}\Delta\right)^2\sqrt{Q}, \tag{15}$$

where $Q = \prod_{\alpha\beta}\prod_{\alpha\beta}$.
From Eq. (8) the relaxation time can be written as

$$\tau = \frac{\Delta t}{\Delta \mathbf{r}^2}3(v) + \frac{1}{2}. \tag{16}$$

If we consider the Smagorinsky sub-grid model, the eddy viscosity should be added to the physical viscosity and the modified relaxation time can be calculated as

$$\tau_{total} = \frac{\Delta t}{\Delta \mathbf{r}^2}3(v + v_t) + \frac{1}{2}. \tag{17}$$

From Eqs. (15) and (17), the modified relaxation time can finally be computed as

$$\tau_{total} = 1/2\left(\sqrt{\tau^2 + \frac{1}{\Delta\mathbf{r}^2}\left(C_{smago}\Delta\right)^2\frac{9\sqrt{8Q}}{\rho}} + \tau\right). \tag{18}$$

As Eq. (18) always has the positive value for the term under the square root, instabilities due to small value of τ will be effectively removed.

2.2. The sediment model

The sole ingredient of the sediment model is sand particle. Sand particles are allowed to move on regular lattice synchronously along with the fluid particles at discrete time steps. But, the presence of the sand particles does not affect the movement (collision and propagation) of fluid particles unless they are part of the bed surface from where fluid particles are bounced back to its original position. As each lattice node is able to contain a multiple number of sand particles and they follow the stochastic rules to change their location, the movement phenomenon can be stated as a representative of multi-particle cellular automata (CA). In this study, the threshold of sediment entrainment similar to those used in traditional scour models [12–16] is introduced in the sediment model. Sand particles are allowed to move from their current positions only if the local Shields parameter is greater than the threshold Shields parameter. The empirical formula for the threshold of sediment particle movement is described below [25]:

$$D_* = \left[\frac{g(s-1)}{v^2}\right]^{1/3}d_{50},$$

$$\theta_{cr} = \frac{0.30}{1 + 1.2D_*} + 0.055\left[1 - \exp\left(-0.020D_*\right)\right],$$

$$\theta_{cr} = \frac{u_{*cr}^2}{g(s-1)d_{50}},$$

where:
D_* = dimensionless grain size,
g = acceleration due to gravity,
s = specific gravity of sediment grains,
v = molecular kinetic viscosity,
d_{50} = median grain diameter,
θ_{cr} = threshold Shields parameter, and
u_{*cr} = threshold friction velocity.
For details regarding the aforementioned equations, readers are referred to [16]. It should be mentioned that all the computations involved in this model are carried out in terms of lattice units unless mentioned otherwise. Therefore, all the physical units are converted into lattice units for the sake of computation. By obeying the rule that the Reynolds numbers in both systems are equal, conversion rules for length scale (L), velocity scale (U) and time scale (t) are set as follows:

$$L^{lattice} = \frac{d^{lattice}}{d^{fluid}}L^{fluid},$$

$$U^{lattice} = \frac{d^{fluid}}{d^{lattice}}\frac{v^{lattice}}{v^{fluid}}U^{fluid},$$

$$t^{lattice} = \left(\frac{d^{lattice}}{d^{fluid}}\right)^2 \left(\frac{v^{fluid}}{v^{latice}}\right) t^{fluid},$$

where, subscript *fluid* represents the physical flow system and subscript *lattice* represents the lattice Boltzmann system.

The macroscopic behavior of scour development is analyzed at mesoscopic level where sand particles follow the rules of transportation, deposition, toppling and scour. It should be mentioned that although all the parameters proposed in this sand model are not fully accurate in representing the microscopic details of the system, the validation of the model for bed profile evolution indicates its strength of predicting scour formation below offshore pipelines. Also, it has been previously demonstrated that macroscopic behavior of a system depends little on the microscopic details [11].

The mesoscopic rules of sand particles are described in the next sections.

2.2.1. Transportation rule

Each lattice node is capable of carrying a certain amount of sand particles. The particle density for a specific node **r** at discrete time step **t** can be expressed as:

$$\rho_p(\mathbf{r}, \mathbf{t}) = \sum_{i=0}^{n} p_i(\mathbf{r}, \mathbf{t}).$$

Particles are allowed to move from the current lattice node to a new location according to the combined action of flow velocity and its own falling speed. Therefore, if one particle is currently staying in location **r** at time **t**, then its new position becomes $\mathbf{r} + \mathbf{c}_i$ based on ($\mathbf{u}_{fluid}(\mathbf{r}, \mathbf{t})$ + $\mathbf{u}_{falling\ speed}$). In fact, the relocation is completed through the stochastic procedure. The directional probabilities of particles are ξ_x, ξy and ξ_z. They can be computed as below:

$$\xi_x = \left|\mathbf{u}_{x,\ fluid} + \mathbf{u}_{x,\ falling\ speed}\right|,$$

$$\xi_y = \left|\mathbf{u}_{y,\ fluid} + \mathbf{u}_{y,\ falling\ speed}\right|,$$

$$\xi_z = \left|\mathbf{u}_{z,\ fluid} + \mathbf{u}_{z,\ falling\ speed}\right|.$$

Finally, the probabilities of moving along various directions can be expressed as:

$$\omega_0 = (1 - \xi_x)(1 - \xi_y)(1 - \xi_z),$$

$$\omega_{xy} = \xi_x \xi_y (1 - \xi_z),$$

$$\omega_{yz} = (1 - \xi_x)\xi_y \xi_z,$$

$$\omega_{zx} = \xi_x(1 - \xi_y)\xi_z,$$

$$\omega_x = \xi_x(1 - \xi_y)(1 - \xi_z),$$

$$\omega_y = (1 - \xi_x)\xi_y(1 - \xi_z),$$

$$\omega_z = (1 - \xi_x)(1 - \xi_y)\xi_z,$$

where, by example, ω_{xy} is the probability to move along xy plane and not along z direction. The exact direction in that plane depends on the sign of the vector **u** $_{fluid}$ + **u** $_{falling\ speed}$. Therefore, once directional probabilities are computed, particles are dispatched from its site **r** to its neighbor nodes ($\mathbf{r} + \mathbf{c}_i$) depending on ω_i. That is the transportation rule for sand particles in a 3–D environment.

2.2.2. Toppling rule

The proposed sand model possesses another important aspect of scour mechanism called toppling. As sand does not have infinite cohesion, stability is lost when particles are piled up excessively on the seabed. In order to maintain the equilibrium condition of particles piling up, their gathering is reoriented. When a specific node contains sand particles excessively, the excess amount of particles is distributed to the left and right neighbors. The excess amount is computed according to the value of angle of repose. Once the excess amount has been sent to the right and left neighbors, the existing amount of particles are again compared with the particle accumulation in the east and west directions. If the site still contains excessive sand particles with respect to east and west neighbors, the excess amount is distributed again. The particle reorientation is not completed in one step. After carrying out numerous numerical tests, it is confirmed that around 10–20 steps of reorientation is required if one step of other mechanisms of morphological seabed change is run.

2.2.3. Deposition

The mechanism of the sand model is implemented maintaining the condition of having three typical lattice nodes in the computational domain. They are: solid nodes, rest particles nodes and fluid nodes. Another important feature of the sand model is threshold of solidification, N_{tresh}. If any lattice node carries N_{tresh} numbers of particles then their accumulation turns the lattice node into solid node which compels all incoming fluid particles to be bounced back. It happens when sand particles are landing on the

bed surface due to the combined action of fluid flow and its own falling speed. The lattice nodes just above the solid nodes are treated as rest particles nodes (or immature solid nodes) where sand particles are arrested to stay on unless the particle amount reaches to N_{tresh} in order to turn the node into solid node. It should be remembered that the rest particles nodes behave like a fluid node having only one exception of not practicing the transportation rule. The presence of sand particles in the fluid node and rest particles node do not interfere with the streaming and collision of fluid particles. It means sand particles of fluid nodes are streaming among the neighbors synchronously along with fluid flow and at the same discrete time step by not affecting the rules of fictitious fluid particles. On the other hand, sand particles of rest particles nodes are unable to head towards neighbor nodes and fluid particles are not affected and remain within their own rules (streaming and collision). So, though (in case of fluid nodes) sand and fluid particles stay together on sites and propagate among neighbor nodes synchronously, their presence does not interfere with each other as they keep themselves in different layers/dimensions.

2.2.4. Scour

The most important feature of the sand model that controls the morphological change of bed is called the scouring mechanism. The scouring mechanism is only valid the top layer of bed nodes and rest particles nodes. The top N_{tresh} particles of the rest particles node and bed node are ejected upward with an erosion probability of $p_{erosion}$. Therefore, specific amount of candidates are selected stochastically to take part in the erosion mechanism. If the shields parameter (θ) in the upper node is higher than the critical shields parameter (θ_{cr}) then candidate particles are washed away according to combined action of fluid flow and falling speed. On the other hand, candidate particles will be sent back to their original nodes if $\theta < \theta_{cr}$. The concept of setting up the threshold of the erosion mechanism is similar to that used in the traditional scour models [12, 13, 15]. This is different from the technique used by Dupuis & Chopard [11].

3. Validation of the flow model

3.1. Lid-driven cubic cavity

Cavity flow driven by a roof lid is well-known as a good benchmark test for numerical and experimental flow research [17–25]. It has been used for many decades in order to validate numerical methods for the prediction of incompressible Navier–Stokes fluid flows. Moreover, it is a popular benchmark problem as it represents complex ge-
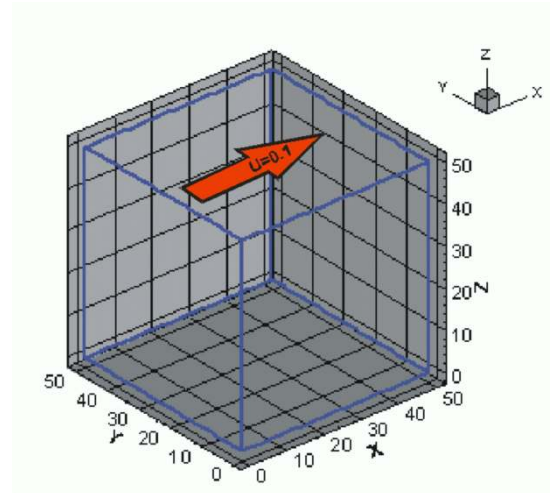

Figure 2. Layout of the domain for flow within a cubic cavity.

ometry flow despite its simple geometry. This is why; first of all, we have selected the lid driven cavity flow problem for validating our LBGK 3-D flow model.

3.1.1. Domain conuration and flow parameters for 3-D cavity flow

In this study, a $51 \times 51 \times 51$ element mesh size is selected for the calculation of the lid-driven flow within a cubic cavity. Fig. 2 depicts the layout of the flow domain where the top lid's speed is, U=0.1 lattice units. The lid is moving along the X direction. No slip boundary condition is considered for each wall except the top wall. Therefore, the velocity boundary conditions on different boundaries are specified as:

$$\left.\begin{array}{l} U_X = 0.1 \, l.u., \\ U_y = 0, \quad \text{and} \\ U_z = 0, \end{array}\right\} \text{top wall}$$

$$\left.\begin{array}{l} U_X = 0, \\ U_y = 0, \quad \text{and} \\ U_z = 0. \end{array}\right\} \text{allother walls}$$

The Reynolds number is calculated based on the velocity of the moving lid and the size of the cavity's edge. Re=400 is considered for the purpose of validating our model as numerical results from various researchers are available at this Reynolds number.

3.1.2. Numerical results for 3-D cavity flow

Fig. 3 plots the simulation results of our model and compares them with the available experimental data [26, 27]. It can be seen that the u and w velocity components taken
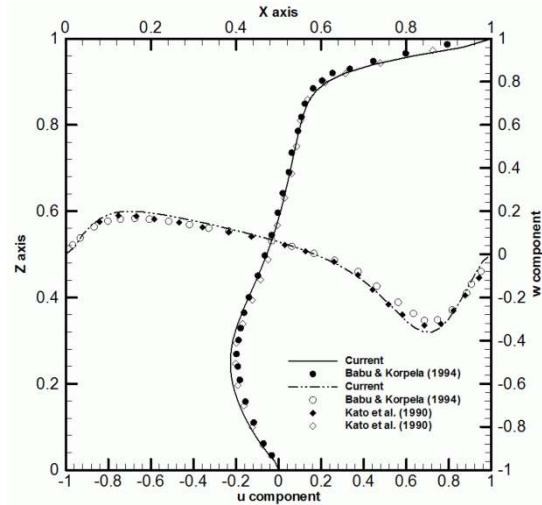
Figure 3. Comparison of u and w velocity profiles in the y-mid plane at Re=400 when grid size is $51 \times 51 \times 51$.
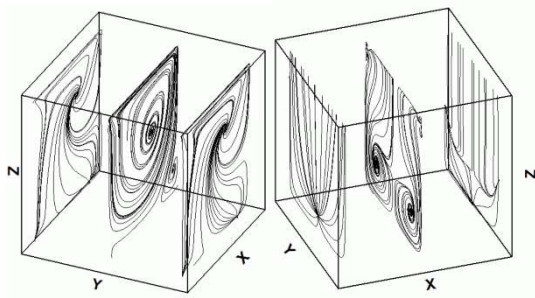

Figure 4. Projections of streamlines onto the end walls and mid-planes of the cavity at Re=400 when lid moves in the x direction (Well compared with (Shanker, 2000)).

Figure 5. Particle tracking presenting downstream secondary eddy (Re=400).

from the y mid–plane compares well with those of other numerical results.

Fig. 4 represents the projected streamlines on the end walls and mid–planes of the cavity domain. The arrangements of the streamlines agree well with those of the numerical results obtained by different researchers [22].

Fig. 5 shows particle tracking originating from the mid-section of y plane and spreading towards the end wall in order to formulate secondary eddy. The orientation of streamlines qualitatively agrees well with the results of [17] obtained at Re=1000.

3.2. Flow around a cylinder

The proposed LBGK 3D flow model is implemented to carry out a numerical test for predicting the three-dimensional vortex shedding flow past an isolated cir-

cular cylinder at a Reynolds number of Re=1000. The main reason for selecting this Reynolds number is that the three–dimensionality is fully developed at this value [28]. Moreover, various experimental results are also available at this Reynolds number which makes us choose this value for validating our numerical results.

3.2.1. Domain configuration

A cuboid flow field is considered for the study of three-dimensional vortex shedding flow around an isolated cir-cular cylinder. The geometry of the computational domain is schematically shown in Fig. 6. The location of lateral boundaries is kept 8D away from the centre of the pipeline. The outflow boundary is located 15D away from the cen-tre of the pipeline. The two–dimensional study carried out by [29] showed that the near wake flow field and the global and local flow parameters of the flow will not be signif-icantly affected by outflow boundary if it is kept 14.5D away from the centerline of the pipe. The pipeline length is considered to be 6.4D. It is reported [28] that there exists two types of vortex shedding modes and their existence is dependent on the Reynolds number. It requires around four cylinder diameters to capture mode A, whilst only about one cylinder diameter is enough to capture mode B. Another study regarding the effect of the spanwise length of the cylinder carried out by [30] showed that the span-wise length less than 2D is not good enough to achieve reliable results. Therefore, the ideal domain width should be about 4D in order to predict three-dimensional vortex shedding flow past an isolated cylinder regardless of the
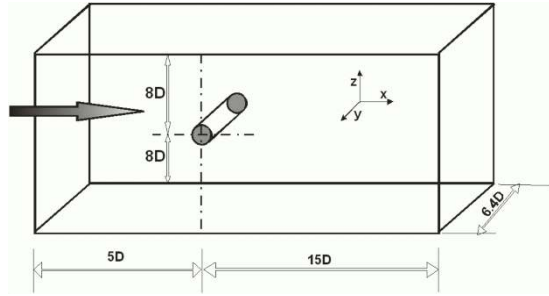
Figure 6. Isometric view of the flow domain.

Reynolds number. So, 6.4D pipe length considered for the present numerical investigation is large enough from all aforementioned aspects.

3.2.2. Boundary condition for the cuboid flow domain

The fluid is assumed to enter into the domain at a uniform velocity. The velocity components are specified as:

$$u = U_o = 0.05, \qquad v = 0. \tag{19}$$

For the flow outlet, the gradients of flow in the longitudinal direction are assumed negligible by imposing the rule as follows:

$$\frac{\partial u}{\partial x} = \frac{\partial v}{\partial x} = 0. \tag{20}$$

The free slip boundary condition is applied at lateral boundaries by using the bounce forward scheme for particle distribution functions.

On the walls of the cylinder surface, the no–slip boundary condition is exercised. Therefore, any particle approaching the wall of the cylinder will be bounced back according to the half–way bounce back scheme. It ensures zero velocity components at wall of the cylinder. In addition, the free–slip boundary condition is also applied on the side walls.

3.2.3. Comparison of hydrodynamic forces

Fig. 7 depicts the timelines of the hydrodynamic forces obtained from the numerical calculations of flow around the isolated cylinder at Re=1000. It is evident that the oscillation of both the drag and lift force coefficients are not regular. Due to the development of 3–D instabilities, the oscillations of both force coefficients are irregular with variable amplitudes. Fig. 7b shows that the oscillation frequency of the lift coefficient is twice the frequency of the drag coefficient. The calculated mean value of drag coefficient is 1.145. It is reported [31] that the mean drag coefficient is 1.1 for Re=1000. On the other hand, the reported [32, 33] experimental measurements of mean drag
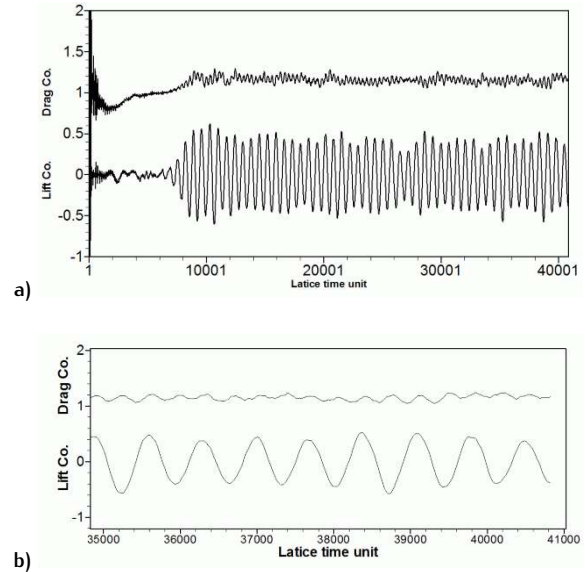

Figure 7. Time histories of hydrodynamic forces.

coefficient lie between 1.0 and 1.20. Therefore, the obtained mean drag coefficient from the present simulation agrees reasonably well with the both numerical and experimental results.

3.2.4. Comparison of Strouhal number

In this study, the vortex shedding frequency is measured in non–dimensional form which is known as Strouhal number. The calculated Strouhal number for Re=1000 is 0.205. On the other hand, the reported [32] Stouhal number at this Reynolds number is 0.20–0.21. Therefore, the predicted Stouhal number is in excellent agreement with the experimental data.

3.2.5. Comparison of spanwise vortices

Fig. 8 describes isosurfaces of spanwise vortices. The numerical results of the current study are presented in Fig. 8a for Re=1000. On the other hand, Fig. 8b depicts numerical results for Re=800. It can be seen that the pattern of spanwise vortices agree well with each other. Though, more three-dimensional effects are revealed in Fig. 8a compared to Fig. 8b. This can be attributed to the difference in Reynolds numbers. Fig. 9 describes the vortex shedding arrangement at randomly selected instances within one cycle of shedding period. It is noteworthy that the vortices are not regular like 2-D vortices. Moreover, the shape of the vortices is also distorted. The irregularity and distortion of vortices appear due to the interaction between the Karman vortices and the three-dimensional vortices developing along the length of the pipe [34].
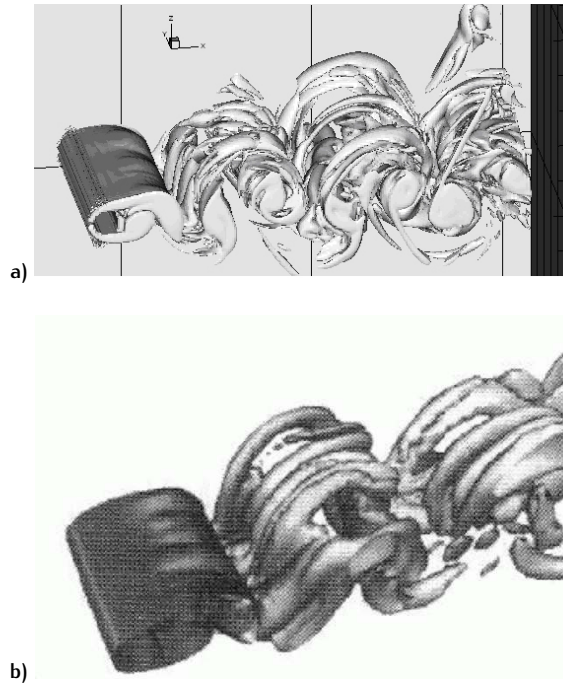
a)

b)

Figure 8. Isosurfaces of spanwise vorticity; a) current study for flow at Re=1000, b simulation results of (Kalro, 1997) for flow at Re=800.

3.2.6. *Comparison of streamwise vortices*

In Fig. 10, the instantaneous velocity vectors along the spanwise direction located at about x/D=1.25 are compared with the numerical results of [35]. The mushroom shaped vortex pairs can be seen in both Fig. 10a and Fig. 10b. Those are characteristic of turbulent flow. Fig. 10 also reveals that the present numerical results are in good harmony with those of [35]. It can also be seen that the counter-rotating vortices are irregular and they cancel each other to merge into a a mushroom-like shape.

4.   Results and discussion

4.1.   Computational domain for modelling 3-D scour

The objective of the present study is to investigate numerically the local flow and scour around pipelines subjected to steady currents. A cuboid computational domain is considered for this purpose where the pipeline is laid directly on a sandy bed (Fig. 11). The pipeline axis is considered to be along the z direction. The flow condition is kept the same as in one of the physical model tests of Mao [2], which is tabulated in Tab. 1. Therefore, the
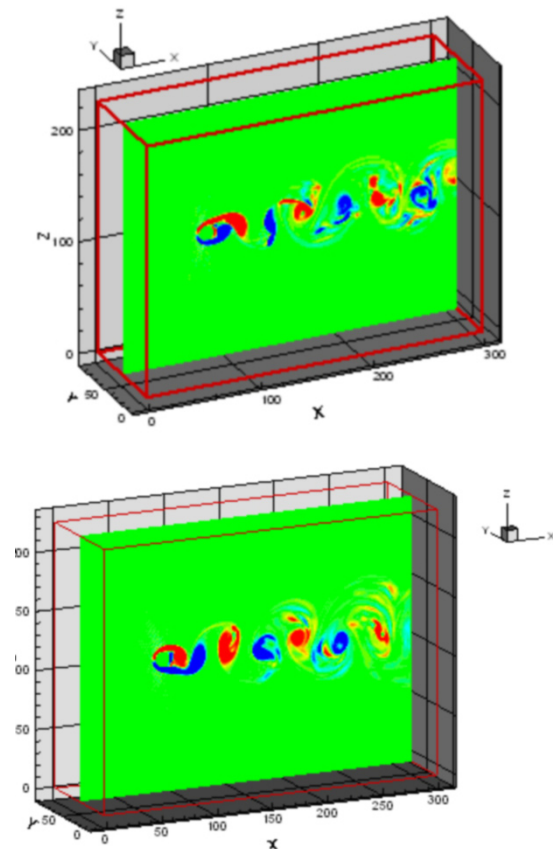
Figure 9. Spanwise vorticity variation at randomly selected instances within one cycle of shedding.

Reynolds number based on the free-stream velocity and pipeline diameter is 50000. A fully developed velocity profile is specified at the left hand side inlet boundary. No slip boundary condition is applied on the pipe surface. At the outflow boundary, zero normal gradient of velocity is implemented. The free slip boundary condition is applied at lateral boundaries by using the bounce forward scheme for particle distribution functions. The mesh density is kept uniform throughout the domain. The diameter of the pipe is 16 lattice units. The pipeline is located at about 6D from the inflow boundary and 12D from the outflow boundary. The depth of water in the computational domain is 3.5D and the height of the sandy bed is 1.0D. The pipeline length is considered as 10.D. The study of [36] suggests that a shorter spanwise extension between $\pi D/2$ and πD is sufficient to accurately predict the 3-D instabilities and all the characteristic components of the flow at a high Reynolds number. Therefore, the consideration of pipe length in this study is large enough to capture the
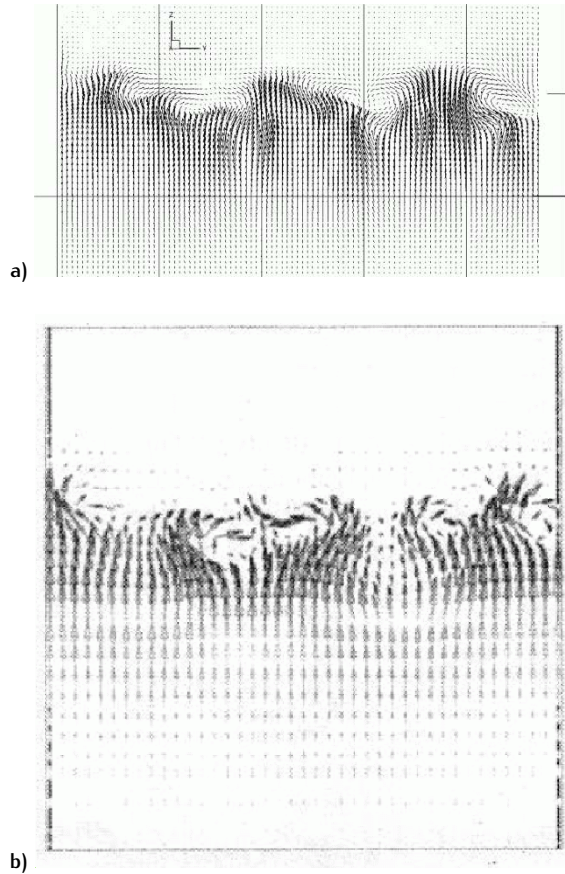
a)

b)

Figure 10. Velocity vectors in spanwise planes; a) result of current model, at Re=1000, b) simulation result of (Kalro, 1997), at Re=800.

Table 1. Configuration of Mao's tests

Pipe diameter (mm)	Sand size d_{50} (mm)	Flow depth (mm)	Flow velocity (mm/s)	Gap ratio (e/D)	Shields parameter (θ)
100	0.36	350	500	0	0.098

three dimensional effects of flow and scour in the vicinity of the pipeline. It should be mentioned that a small gap is purposely included between the pipeline and the sandy bed at the middle of pipeline. The dimension of the gap is $1.0D \times 1.0D \times 0.1D$. The purpose of it is to allow the scour to develop towards both ends of the pipeline.

4.2. Model parameters

The characteristic grain size of sand material is considered as a constant in the current study. Therefore, the
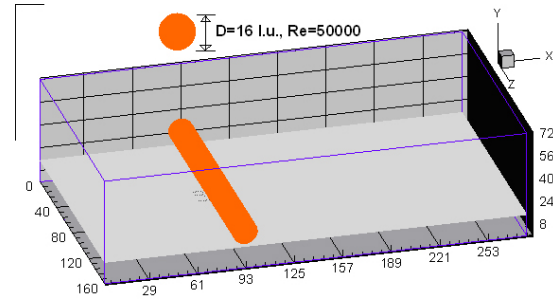
Figure 11. Computational domain for simulating 3-D flow and scour around offshore pipelines.

amount of sand particles in one lattice node is fixed assuming that the sand particle is uniform. The falling speed ($\mathbf{u}_{falling\,speed}$) of the sand particles and probability of erosion ($p_{erosion}$) are all in real units. Like Dupuis and Chopard [11], we consider the value of falling speed, $\mathbf{u}_{falling\,speed} = 0.06 \times U_0$. In the current study, $p_{erosion}$ is chosen as 0.05. As the calculation results agree with the experimental results, the chosen values of LBM parameters proves its capability to model the evolution of scour formation under submarine pipelines. For details regarding the selection of the value of $\mathbf{u}_{falling\,speed}$ and $p_{erosion}$ readers are referred to [11].

4.3. Prediction of scour development

The purpose of this paper is to study three-dimensional scour processes employing our proposed 3-D scour model. Additionally, numerical results obtained from the developed model will also be validated against experimental observations and test results available in literature.

4.3.1. Observation of spiral vortex

The study of three-dimensional scour carried out by [37] revealed that a spiral type vortex may exist in front of the pipeline. They claimed that the presence of this type of vortex is generated due to the three dimensional separation under the adverse pressure gradient produced by the pipe in which the separated boundary layer rolls up. Our numerical investigation of flow and scour around pipelines confirms that there certainly exists a spiral type vortex located in front of the pipe. Fig. 12 shows the existence of such a vortex that has developed in the vicinity of the pipe. The formation process of the vortex is similar to the formation of horseshoe vortex around a pile [37]. In Fig. 12a, the pipeline is purposely not presented whereas in Fig. 12b the pipeline is presented. Fig. 12a shows that the three dimensional effect exists all around the domain except in the middle part of the scour hole. The streamline nearly in

the middle part of the scour hole propagates from the bottom of the scour hole to the downstream side maintaining an almost 2-D nature. This 2-D propagation of streamlines is more pronounced when the scour is developing significantly towards the streamwise direction. Fig. 13b shows that the two dimensional propagation of streamlines along the streamwise direction at the equilibrium stage. It also reveals that the 2-D propagation of streamlines is more pronounced in the middle part of the scour hole than the previous case. It confirms that the scour is a two-dimensional process in the middle part of the scour hole. On the other hand, the three-dimensional propagation of streamlines near the shoulder of span (Fig. 12, Fig. 13b) confirms the presence of thee-dimensional nature of scour around it.

4.3.2. Development of scour hole and the regime of 2-D scour

Fig. 12 shows the scour hole shape at an early stage of development of the scour. It reveals that the propagation rate of scour is higher along streamwise direction than that along spanwise direction. This is due to the presence of a stronger velocity component along the streamwise direction, which allows the sand particles to move mainly in this direction. Fig. 13 shows the equilibrium scour hole shape of the sandy bed. It can be seen that the spanwise propagation of scour extends towards both ends of the pipe almost equally. This can be attributed to the zero degree angle of inclination considered in this case of Mao's experiment. Fig. 13b shows streamlines at different locations of the scour hole. The streamlines that pass near the span shoulder of the pipe are not parallel to each other due to the strong 3-D effects of flow in this region. On the other hand, the streamlines in the middle of the scour hole stay almost parallel to each other. This indicates that the scour is a 2-D process in the middle of the suspended pipe. The critical regime of 2-D scour process is found to be up to 1.0D away from the middle of the suspended span in both directions.

4.3.3. Section- wise analysis of scour development

Fig. 14 and Fig. 15 show groups of various cross sections of equilibrium scour bed presented in streamwise and spanwise directions respectively. The blue color in those figures represents fluid whereas the ash color represents sandy bed or pipe. It is obvious that the maximum scour along spanwise direction belongs to the plane of pipe axis. On the other hand, the x-y plane which passes through the middle section of the suspended span represents maximum erosion that has taken place along streamwise direction. Fig. 16 shows various cross sections of equilibrium scour bed along streamwise directions. The cross sections of
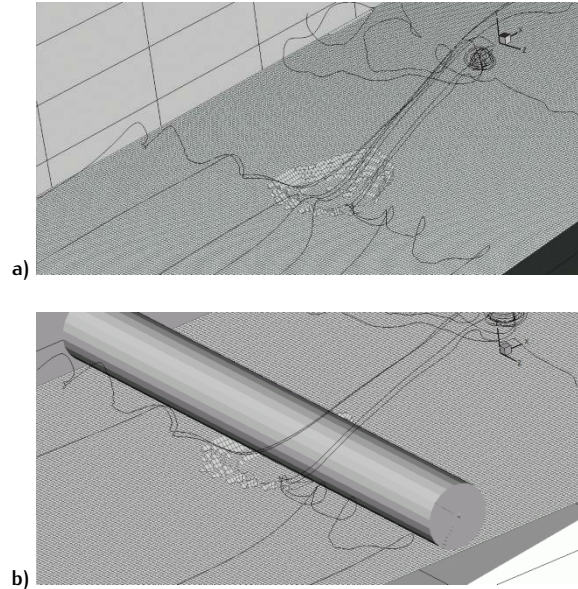

Figure 12. Streamlines in a scour bed at a randomly selected stage of time development of scour.

scour hole shape located at various positions from the mid span of the suspended pipe to the left end of the pipe are presented in Fig. 16. It can be seen that the maximum scour depth happens at the mid-section of the suspended pipe. The scour hole depth reduces as the distance between the streamwise cross section and the mid section of the pipe increases. This is due to the generation of a stronger vortex shedding flow at the mid-section plane of the suspended pipe with respect to that in the vicinity of the span shoulder.

Fig. 17 shows various cross sections of equilibrium scour bed along the spanwise direction. It can be seen that the maximum scour occurs along the pipe axis. Fig. 17 also reveals that the maximum scour depth takes place directly underneath the pipe. Additionally, scour hole depth reduces as the distance between pipe axis and the considered cross-sectional plane normal to the main flow increases.

Fig. 18 presents the shapes of the equilibrium scour hole at different cross sections along streamwise direction. The streamlines are also presented along with the scour bed. It can be seen that there exists the generation of vortex shedding in every section. It is believed that vortex shedding generation is responsible for the lee-wake erosion and that has been confirmed through Fig. 18.

4.3.4. Comparison of bed profiles

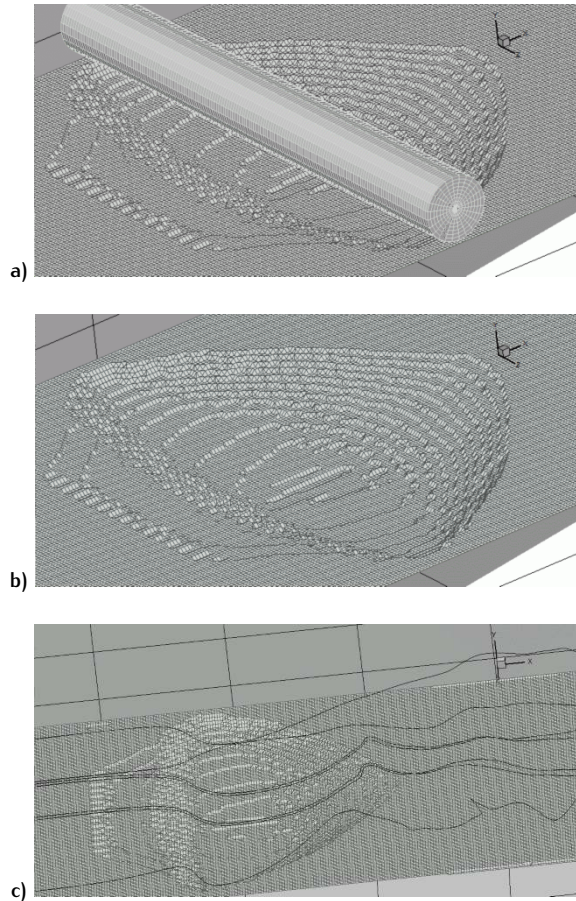Fig. 19 shows the comparison of bed profiles with the numerical results of Mao's experiment. It should be noted

a)

b)

c)

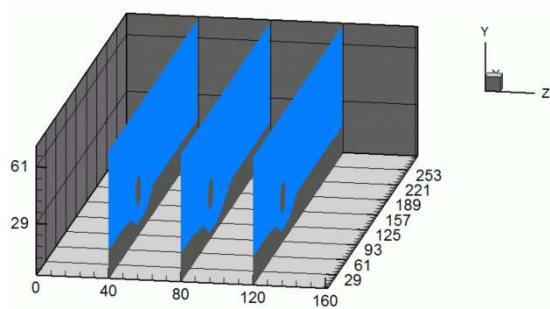**Figure 13.** Equilibrium scour bed profiles presented with or without cylinder and selected streamlines.

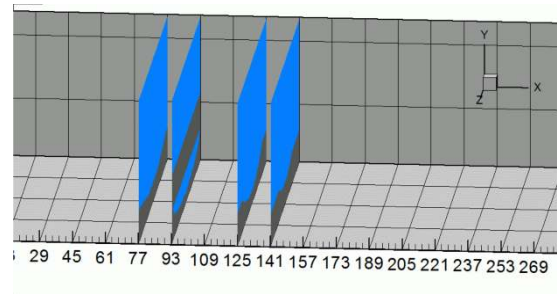**Figure 14.** Equilibrium bed profiles along streamwise direction, D=100 mm, gap-to-diameter ratio=0, Re=50000.
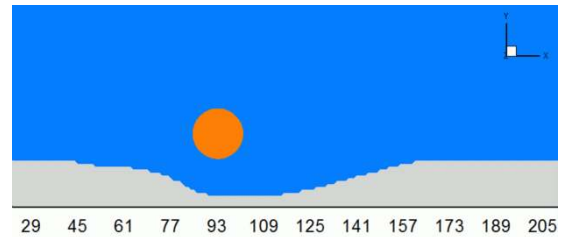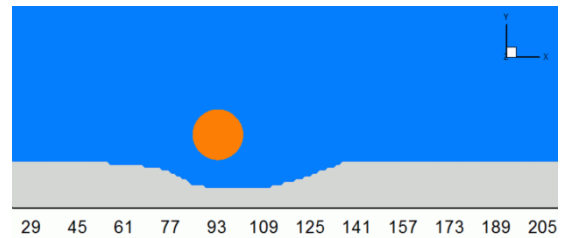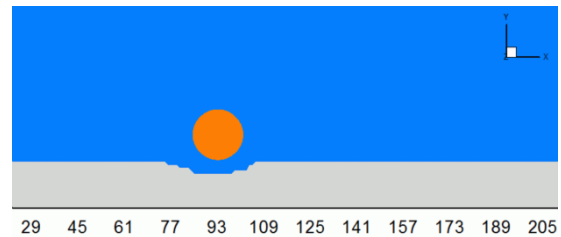

Figure 15. Equilibrium bed profiles along spanwise direction, D=100 mm, gap-to-diameter ratio=0, Re=50000.

a) Mid section, z=80

b) Z=120

c) Z=145

Figure 16. Equilibrium bed profiles at various sections of the computational domain.

that the bed profiles in Fig. 19 represent the cross-sectional plane parallel to the main flow which passes through the middle section of the suspended span. It can be seen that the present numerical model is not able to predict the early stage of the scour development very well. The predicted scour depth is smaller than that of measured

depth of Mao's experiment. This discrepancy happens as the numerical model in this study reveals weaker tunnel scouring underneath the pipeline. Apart from that, the predicted equilibrium scour profiles of the present numerical model agree very well with those measured in experiment. Fig. 19c confirms that the predicted time devel-
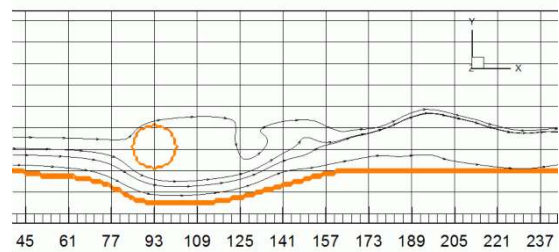
a) X=93

b) X=125

c) X=141

Figure 17. Equilibrium bed profiles at various sections of the computational domain.

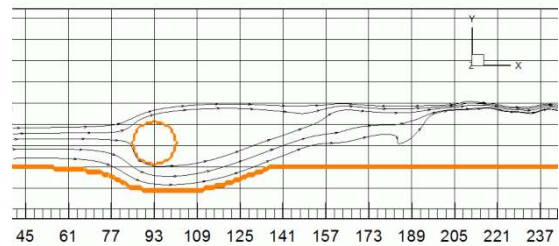**a)** Z=80

b) Z=120

c) Z=40

Figure 18. Streamlines for equilibrium bed profiles at various sections of the computational domain.

opment of the maximum scour depth is in fair agreement with that of Mao's experiment. Additionally, the equilibrium scour hole shape in the vicinity of the suspended pipe is agrees well with that in Mao's experiment. It reveals that the present 3-D model predicts the lee-wake scour quite well.

Dey and Singh [38] conducted few experiments on clear-water scour below underwater pipelines in uniform and non-uniform sediments under steady flow. In our test case, we consider the depth of flow to be 350 mm, incoming fluid velocity as 500 mm/s, pipe diameter as 100 mm and d_{50} of sand as 0.36 mm. The test case of Dey & Singh [38], which is close to our numerical test case, represents the depth of flow as 280 mm, incoming flow velocity as 28.3 mm/s, pipe diameter as 70 mm and d_{50} of sand as 0.48 mm. According to their experimental observations, the maximum depth of scour is 69 mm which represents around 98 percent of the diameter of the pipe. On the other hand, according to

our numerical investigation, the maximum scour depth is around 80 percent of the diameter of the pipe. Therefore, for both cases, the maximum scour depth is less than the diameter of the pipe and agrees well with each other.

4.3.5. Scour propagation speed along the pipeline

The research regarding the experimental investigation of propagation scour along offshore pipelines has not been not far-reaching until now. Though, Leeuwestein *et al.* [39] gave an account of the propagation scour along the spanwise direction, their research emphasis was mainly on stability and self-burial of pipeline. In the PhD thesis of Yeow [40], extensive experimental investigations are carried out regarding the three-dimensional local scour below pipelines. In his PhD thesis, significant research emphasis is given to investigating the propagation speed of scour hole along the pipeline length subjected to steady currents. In his experimental observations for the cases with
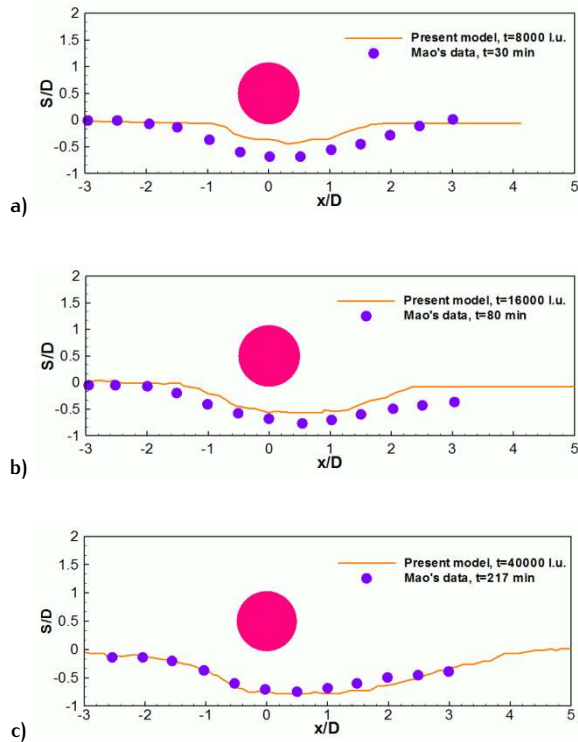
Figure 19. Comparison of scour hole shapes with experimental data, D=100 mm, gap-to-diameter ratio=0, Re=50000.

Figure 20. Propagation of scour hole along spanwise direction.

zero degree incident angle, it is revealed that the scour propagates from the middle part of the free span to each end of the pipeline at a constant rate or at two constants rates. He concluded that the free span length increases almost linearly with time until it reaches both ends of the pipeline. It should be mentioned that the current numerical results obtained from the investigation regarding propagation speed of scour along the pipeline length is consistent with the experimental observation of Yeow. Fig. 20 presents L/D *versus* lattice unit of time where L/D represents the free span length measured from the middle part of the pipeline to nearest support point of the pipe on the lefthand side. It can be seen that there exists an almost constant rate of propagation of scour along the spanwise direction, which is consistent with experimental observation of Yeow [40]. This represents the robustness of the current numerical model.

4.3.6. Analysis of scour hole slope at transverse direction

Fig. 21 shows various cross sections of the scour hole shapes developed at different stages of scour process along the length of the pipe. It is revealed that the spanwise propagation rates of scour hole towards right
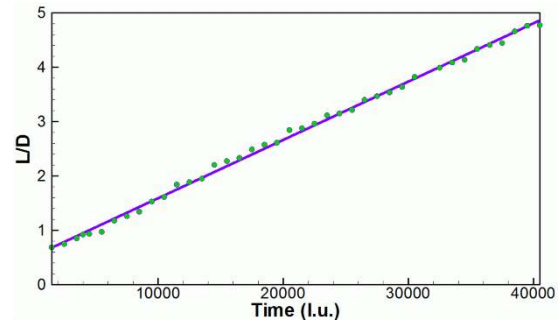
and left ends of the pipelines are almost the same. This type of scouring happens as the flow is perpendicular to the pipeline. Fig. 21 also reveals that the scour slope at the shoulder region remains fairly constant throughout the whole scour process. The fairly constant slope of the scour hole expressed through the Fig. 21 also suggests that the natural angle of repose of the sand might be a fair estimate for transverse scour slope.

5. Conclusions

A three-dimensional flow and scour model is developed in this chapter in order to predict lattice unit time-dependent scour below pipelines. Based on the research findings in this paper, the following conclusions can be drawn:

1. The 3-D flow model predicts the gross features of 3-D cavity flow and the flow around an isolated circular cylinder quite well.

2. The existence of a spiral vortex in the proximity of the span shoulder is confirmed by the simulation results of our numerical model.

3. The critical regime of the 2-D scour process is found to be up to 1.0D away in both directions from the middle of the unsupported length of pipelines.

4. The equilibrium maximum scour depth and the shape of equilibrium scour hole compare well with the available experimental data.

5. The speed of propagation of scour along the pipeline length maintains an almost constant rate, which is consistent with the experimental observations of Yeow [40].

6. The existence of vortex shedding is demonstrated by the simulation results. This confirms that the vortex
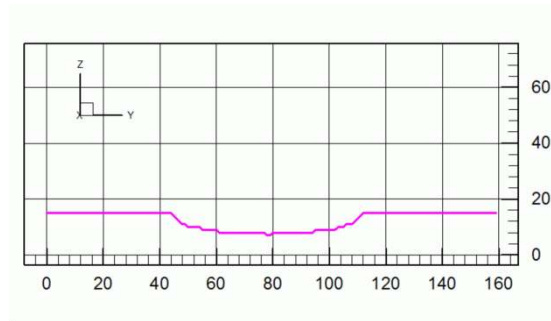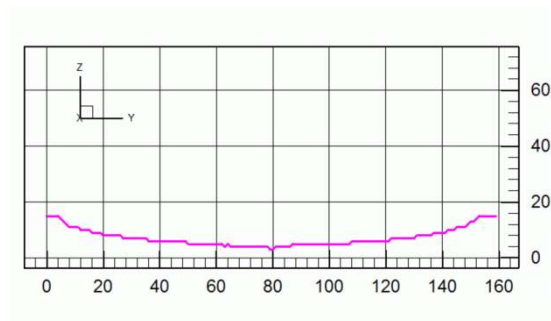
a) Steps=16000
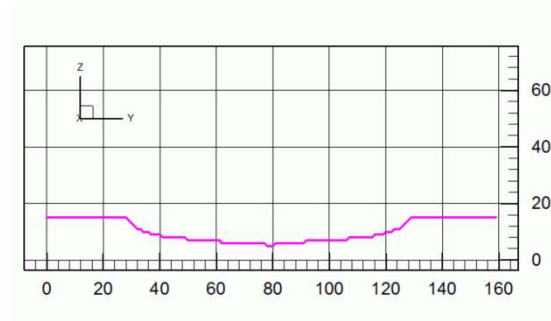
b) Steps=26000
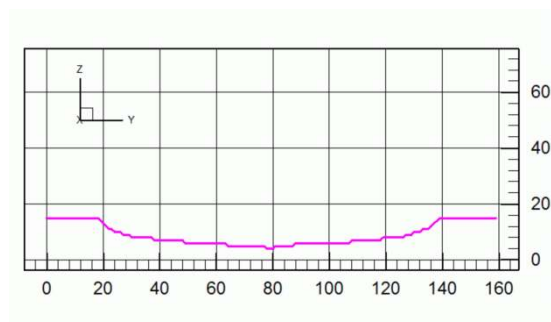
c) Steps=32000

d) Steps=40000

Figure 21. Streamlines for equilibrium bed profiles at various sections of the computational domain.

shedding plays important role for the generation of lee-wake scour.

7. The scour slope at the shoulder region remains fairly constant throughout the whole scour process.

8. The scour process along the streamwise direction is stronger than that of the spanwise direction.

Acknowledgements

References

[1] R. Bruschi, M. Drago, M. Venturi, G. Jiao, T. Sotberg, Pipeline reliability across erodible/active seabeds, Proceedings of 1997 Offshore Technology Conference, Houston, Texas, USA, OTC 8493 (1997)

[2] Y. Mao, The interaction between a pipeline and an erodible bed, Series Paper, Institute of Hydrodynamics and Hydraulic Engineering, Technical University of Denmark (1986)

[3] B. M. Sumer, H. R. Jensen, Y. Mao, J. Fredse, J. Waterway Div.-ASCE 114, 599 (1988)

[4] B. M. Sumer, C. Truelsen, T. Sichmann, J. Fredsoe, Coast. Eng. 42, 313 (2001)

[5] F. P. Gao, B. Yang, Y. X. Wu, S. M. Yan, Appl. Ocean Res. 28, 291 (2006)

[6] S. Ushijima, J. Comput. Phys. 125, 71 (1996)

[7] P. L. Bhatnagar, E. P. Gross, M. Krook, Phys. Rev. 94, 511 (1954)

[8] D. Yu, R. Mei, L. Lou, W. Shyy, Prog. Aerosp. Sci. 39, 329 (2003)

[9] A. Dupuis, PhD thesis, University of Geneva (Geneva, Switzerland, 2002)

[10] S. Hou, J. Sterling, S. Chen, G. D. Doolen, Theoretical Division and Center for Nonlinear Studies, Los Alamos National Laboratory, Los Alamos, NM 87545 (1994)

[11] A. Dupuis, B. Chopard, J. Comput. Phys. 178, 161 (2002)

[12] D. Liang, L. Cheng, Li. F., Coast. Eng. 52, 43 (2005)

[13] F. Li, L. Cheng, J. Waterway Div.-ASCE 127, 106 (2001)

[14] F. Li, L. Cheng, J. Hydraul. Eng.-ASCE 125, 400 (1999)

[15] B. Brors, J. Hydraul. Eng.-ASCE 125, 511 (1999)

[16] R. Soulsby, Dynamics of marine sands: a manual for practical applications (Thomas Telford Publications, London, 1997)

[17] Z. Zunic, M. Hribersek, L. Skerget, J. Ravnik, 3D lid driven cavity flow by mixed boundary and finite element method, European Conference on Computational Fluid Dynamics, TU Delft, The Netherlands, 2006 (2006)

[18] C. K. Aidun, N. G. Triantafillopoulos, Phys. Fluids 3, 2081 (1991)

[19] J. R. Koseff, R. L. Street, J. Fluid. Eng.-T. ASME 106, 390 (1984)

[20] A. K. Prasad, J. R. Koseff, Phys. Fluids 1, 208 (1989)

[21] T. W. H. Sheu, S. F. Tsai, Comput. Fluids 31, 911 (2002)

[22] P. Shanker, M. D. Deshpande, Annu. Rev. Fluid Mech. 32, 93 (2000)

[23] J.-L. Guermond, C. Migeon, G. Pineau, L. Quartapelle, J. Fluid Mech. 450, 169 (2002)

[24] A. R. Davies, J. L. Summers, Wilson, M.C.T., Parallel Computaional Fluid Dynamics-New Frontiers and Multi-Disciplinary Applications, 265 (2003)

[25] G. Guj, F. Stella, J. Comput. Phys. 106, 286 (1993)

[26] Y. Kato, H. Kawai, T. Tanahashi, JSME Int. J. II-Fluid. 33, 675 (1990)

[27] V. Babu, S. A. Korpela, Comput. Fluids 23, 675 (1994)

[28] C. H. K. Williamson, Annu. Rev. Fluid Mech. 28, 477 (1996)

[29] T. E. Tezduyar, R. Shih, J. Eng. Mech.-ASCE 117, 854 (1991)

[30] C. Lie, L. Cheng, K. Kavanagh, Comput. Method. Appl. M. 910, 2909 (2001)

[31] R. D. Henderson, J. Fluid Mech. 352, 65 (1997)

[32] M. Braza, P. Chassaing, Ha H. Minh, J. Fluid Mech. 165, 79 (1986)

[33] H. J. Niemann, N. Holscher, J. Wind Eng. Ind. Aerod. 33, 197 (1990)

[34] C. Lei, PhD thesis, University of Western Australia (Crawley, Australia, 2000)

[35] V. Kalro, T. Tezduyar, Parallel Comput. 23, 1235 (1997)

[36] D. F. L. Labble, P. A. Wilson, J. Fluid. Struct. 23, 1168 (2007)

[37] B. M. Sumer, J. Fredsoe, The Mechanics of Scour in the Marine Environment (World Scientific, Singapore, 2002)

[38] S. Dey, N. P. Singh, J. Hydraul. Eng.-ASCE 134, 588 (2008)

[39] W. Leeuwestein, E. W. Bijker, E. B. Peerbolte, H. G. Wind, The natural selfburial of submarine pipelines, Proc 4th Int. Conf. on behaviour of offshore structure (Elsevier, 1985) 717

[40] K. Yeow, PhD thesis, The University of Western Australia (Perth, Australia, 2007)